

Decoupling fast hydrogen oxidation reaction on a tandem electrocatalyst

Received: 3 February 2025

Accepted: 15 July 2025

Published online: 22 July 2025

Check for updates

Wei Guo¹, Guoqiang Zhao^{2,3}, Ziang Sun⁴, Bingxing Zhang¹, Dongyue Xin⁵, Mingxia Gao¹, Yongfeng Liu¹, Zhongbin Zhuang⁵, Hai-Wei Liang⁴, Hongge Pan^{1,6} & Wenping Sun^{1,7} ✉

The hydrogen oxidation reaction (HOR) shows fast kinetics in proton exchange membrane fuel cells (PEMFCs), and has not drawn intense attention. Here, we propose a tandem electrocatalysis concept, decoupling HOR on two independent active sites for accelerated kinetics. As a proof-of-concept application, a Ru-based tandem HOR catalyst is designed, with Ru nanoclusters decorated with Pt single atoms. Experimental and theoretical studies suggest that H₂ dissociation occurs at Ru sites, and then the produced H species migrate to Pt sites followed by the desorption of H⁺. The strong Ru-H interaction promotes the H₂ dissociation step, while the optimum Pt-H interaction ensures the fast desorption, thereby substantially enhancing the HOR kinetics. In H₂-O₂ fuel cells, this catalyst enables a peak power density of 1.91 W cm⁻² and a high anodic mass activity of 23.12 A mg⁻¹ at 0.9 V_{ir-free} with an ultralow noble metal loading of 5 μg cm⁻². This work advances the development of low-cost anode catalysts for fuel cells and provides more insight into understanding hydrogen electrocatalysis.

Proton exchange membrane fuel cells (PEMFCs) are typical energy conversion devices that can produce electricity using hydrogen as the fuel for a variety of applications, including transportation, industry, aerospace, etc.^{1–11} One major hindrance to the commercial implementation of PEMFCs is the substantial cost associated with the high-loading platinum (Pt) catalysts in both anode and cathode.^{12–18} The U.S. Department of Energy has set an ambitious target for platinum group metal (PGM) loading in PEMFCs at 0.1 mg/cm² by 2025,¹⁹ a benchmark that current catalysts struggle to meet.^{12,20} Typically, the required amounts of Pt are 0.02–0.05 and 0.1–0.3 mg cm⁻² for the anodic hydrogen oxidation reaction (HOR) and the cathodic oxygen reduction reaction (ORR), respectively.^{20–25} The higher Pt demand at the cathode has attracted intense interest, aiming to improve the specific activity of Pt for the ORR,²⁶ and the Pt loading at the cathode has been

dramatically decreased from over 2 to 0.1 mg/cm² over the past decades.^{12,20,21,27} In contrast, increasing the HOR activity of Pt and hence reducing the Pt loading at anode side has received very limited attention,^{28–31} and there still remains much space to further reduce the usage of Pt at the anode side.

The HOR process in acidic media is generally considered to involve the adsorption and dissociation of H₂ followed by the desorption of hydrogen species (H*) to produce H⁺ on one single active site, and the adsorbed H* is the only reaction intermediate.³² Based on the Sabatier's principle,³³ Pt serves as the most active acidic HOR catalyst due to its optimum hydrogen binding energy (HBE).^{4,34–36} Very few non-Pt catalyst systems were reported for the acidic HOR, and most traditional design strategies focus on optimizing the HBE by regulating the local structure of active sites.²¹ Basically, strong hydrogen bonding

¹School of Materials Science and Engineering, Zhejiang University, Hangzhou, P. R. China. ²Engineering Research Center of Nano-Geomaterials of Ministry of Education, China University of Geosciences, Wuhan, P. R. China. ³Faculty of Materials Science and Chemistry, China University of Geosciences, Wuhan, P. R. China. ⁴Department of Chemistry, University of Science and Technology of China, Hefei, P. R. China. ⁵State Key Lab of Organic-Inorganic Composites and Beijing Advanced Innovation Center for Soft Matter Science and Engineering, Beijing University of Chemical Technology, Beijing, P. R. China. ⁶Institute of Science and Technology for New Energy, Xi'an Technological University, Xi'an, P. R. China. ⁷State Key Laboratory of Clean Energy Utilization, Zhejiang University, Hangzhou, P. R. China. ✉e-mail: wenpingsun@zju.edu.cn

could promote the dissociation of H_2 , but is not beneficial to the H^* desorption, thereby slowing down the overall HOR kinetics. We hypothesize that, catalytic performance breakthrough can be anticipated if the HOR process is decoupled, with H_2 dissociation and H^* desorption happening on two independent preferred active sites. More significantly, this kind of catalyst system might allow for the use of some much cheaper metals that possess strong affinity with hydrogen, for example, Ru,³⁷ and in turn greatly reduces the required amount of Pt.

Herein, we propose a concept of tandem electrocatalysis to decouple the HOR process toward faster reaction kinetics, and develop a highly efficient tandem HOR electrocatalyst, with Ru nanoclusters (NCs) decorated with Pt single atoms (denoted as Pt1-Ru/C). Experimental results evidence the decoupling of the HOR, and the isotope test and the in situ infrared spectroscopy demonstrate the hydrogen spillover from Ru sites to Pt sites. The theoretical calculations confirm the thermodynamic advantages and feasibility of the tandem electrocatalysis mechanism on this unique catalyst. Accordingly, the Pt1-Ru/C anode catalyst with ultra-low PGM content ($5 \mu\text{g}_{\text{PGM}} \text{cm}^{-2}$) delivers a peak power density (P_{max}) of 1.91 W cm^{-2} and reaches a high anodic mass activity of $23.12 \text{ A mg}^{-1}_{\text{PGM}}$ at $0.9 V_{\text{IR-free}}$ in PEMFCs.

Results

Structural characterization of Pt1-Ru/C

The Ru/C and Pt1-Ru/C catalysts were synthesized via a conventional wet impregnation process (see Experimental Section for details). The X-ray diffraction (XRD) patterns (Supplementary Fig. 1) show no typical diffraction peaks for Ru and Pt. The high-resolution transmission

electron microscopy (HRTEM) images reveal that the metallic Ru exists in the form of clusters with size of around 1.5 nm (Fig. 1a and Supplementary Figs. 2–5) for Pt1-Ru/C catalyst. The results of inductively coupled plasma mass spectrometry indicate that the Ru content in the samples is approximately 1.0 wt%, and the Pt content in Pt1-Ru/C is 0.14 wt% (Supplementary Table 1).

The energy dispersive X-ray spectroscopy (EDS) mappings and the EDS line-scanning profile (Supplementary Fig. 6) confirm the concentrated distribution of Pt elements on Ru NCs. As can be seen from the aberration-corrected high-angle annular dark-field scanning transmission electron microscopy (HAADF-STEM) image and the intensity profiles (Fig. 1b, c), Pt species exists as single atoms anchored on Ru NCs. The Ru valence state of Pt1-Ru/C increases as compared with Ru/C (Supplementary Figs. 7 and 8), indicating that electron transfer from Ru to Pt occurs.³⁸ The extended X-ray absorption fine structure (EXAFS) spectra and fitting results, analyzed with Demeter software,³⁹ are presented in Supplementary Figs. 9 and 10 and Supplementary Tables 2 and 3, respectively. Pt species are in the form of Cl-coordinated single atoms in Pt1-Ru/C (Fig. 1d, e and Supplementary Fig. 11), which has negligible effect on the coordination structure of Ru NCs (Supplementary Fig. 12 and Supplementary Table 2).

A series of ex situ characterizations were employed to monitor the structural changes of the catalyst during the HOR process. The catalyst was coated on carbon fiber papers. After the catalyst was activated (referred to as Pt1-Ru/C-A) at an overpotential of 0.1 V for 3 h, the coordination and electronic structure of Ru almost remains unchanged (Supplementary Figs. 13–15 and Supplementary Table 2). In contrast, the oxidation state of Pt single atoms greatly decreases

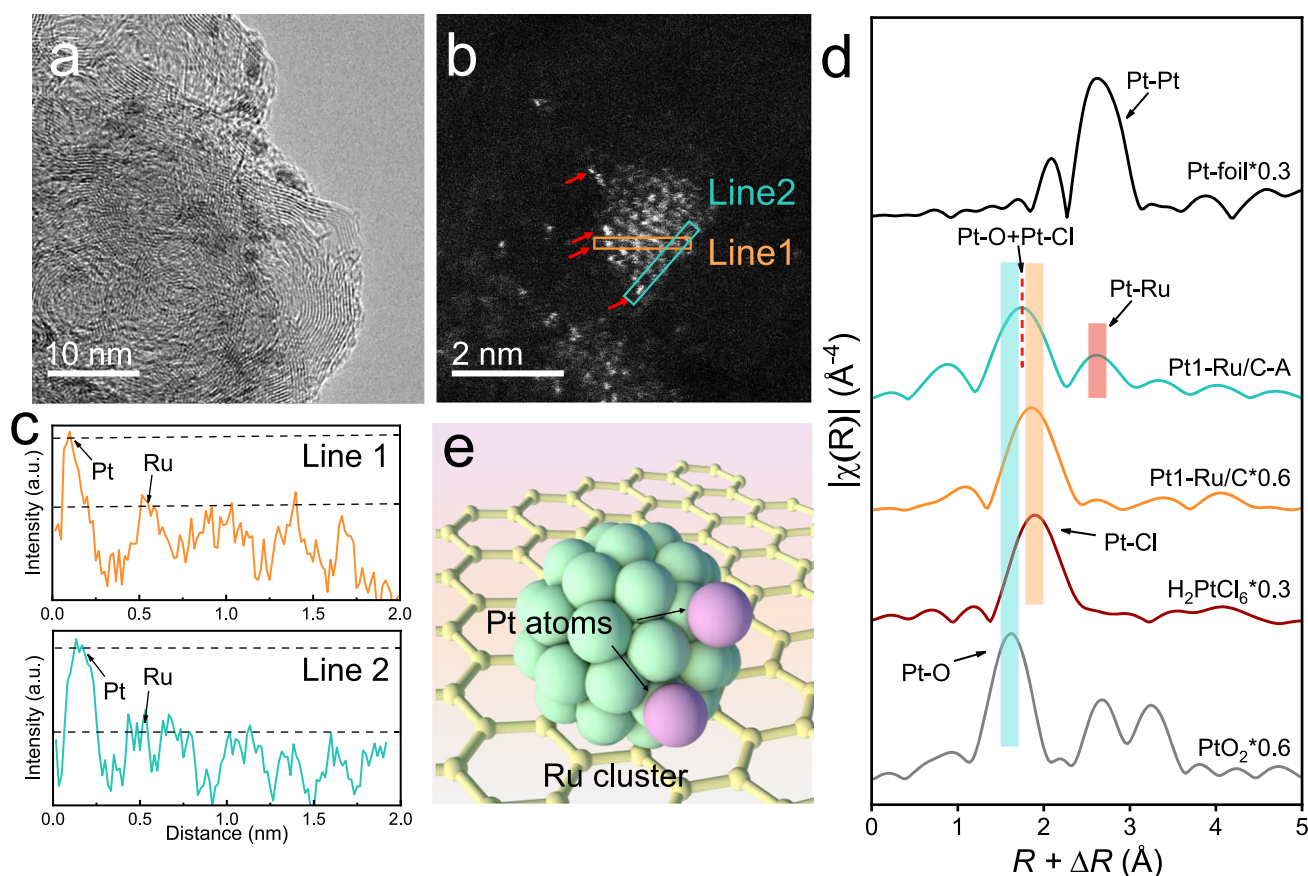


Fig. 1 | Electro-catalysts morphology and structure characterization. **a** HRTEM image, **b** HAADF-STEM image, and **(c)** the intensity profiles along lines 1 and 2 in Fig. 1b of Pt1-Ru/C. **d** Pt L_3 -edge EXAFS spectra of Pt-foil, Pt1-Ru/C-A, Pt1-Ru/C, H_2PtCl_6 , and PtO_2 . **e** the schematic illustration of Pt1-Ru/C catalyst structure, in

which the green clusters denote Ru clusters, the purple spheres represent Pt atoms, and the light green spheres correspond to C atoms. Source data are provided as a Source Data file.

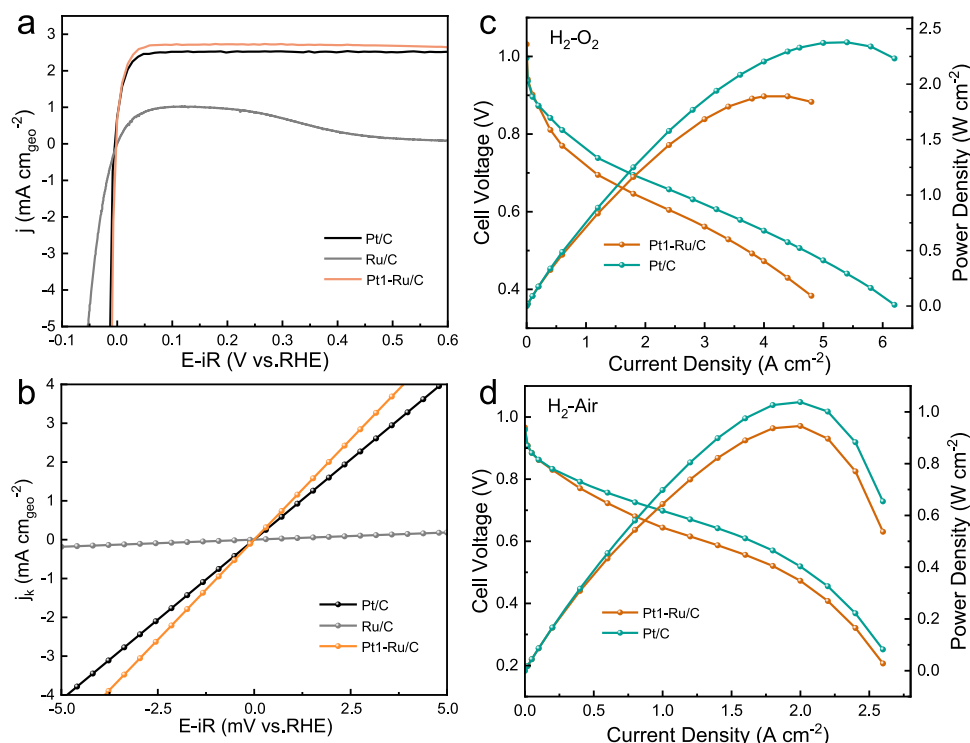


Fig. 2 | Electrochemical HOR and PEMFCs performance. **a** Geometric area-normalized LSV curves of different catalysts. **b** Linear region of kinetic current density (j_k) (calculated based on the Koutecky–Levich equation). All LSV curves were collected at a scan rate of 0.5 mV s^{-1} with 90% iR compensation on a RDE at 1600 rpm. The ohmic resistance ($5 \pm 0.3 \Omega$) for iR compensation was obtained from EIS analysis with a geometric area of 0.19625 cm^2 . The PEMFC polarization and power density curves were recorded with anode PGM loadings of $0.005 \text{ mg}_{\text{PGM}} \text{ cm}^{-2}$ for Pt1-Ru/C

and $0.05 \text{ mg}_{\text{Pt}} \text{ cm}^{-2}$ for commercial Pt/C under $\text{H}_2\text{-O}_2$ (c) and $\text{H}_2\text{-air}$ conditions (d). Conditions for all the fuel cell tests: commercial Pt/C cathode catalyst with a loading of $0.1 \text{ mg}_{\text{Pt}} \text{ cm}^{-2}$, 80°C , 100% relative humidity, absolute pressure of 250 kPa, H_2 , O_2 , and air with flow rates of 1.0, 2.0, and 2.0 L min^{-1} , respectively, unless otherwise stated. The PEMFC polarization curves are not iR-corrected. Source data are provided as a Source Data file.

(Supplementary Figs. 14 and 15 and Supplementary Table 4) with enhanced Pt-O coordination (Fig. 1d, Supplementary Fig. 11, and Supplementary Table 3), indicating that Pt is further reduced and converted into oxygen-coordinated single atoms during the HOR process.

The continuous Cauchy wavelet transform (CCWT) analyses were performed to provide more insights into the coordination structure. As demonstrated in the Supplementary Figs. 16–18, the absence of detectable metal-metal coordination in the Pt1-Ru/C catalyst indicates that the initial Cl-coordinated Pt single atoms are adsorbed on Ru NCs without forming chemical bonds. After the activation, as depicted in Fig. 1d, a distinct metal-metal coordination at 2.65 \AA in R-space emerges in the Pt1-Ru/C-A sample, the position of which in k-space (7.0 \AA^{-1}) is lower than the Pt-Pt bond in Pt-foil (9.8 \AA^{-1}) (Supplementary Figs. 17 and 18). The downshift in k-space generally indicates the presence of lighter elements in the coordination shell.⁴⁰ In our case, the results suggest the formation of Pt-Ru bonds, which probably originates from the activation process that induces the structural reorganization of Pt1-Ru NCs.⁴¹

HOR and PEMFCs performance

The HOR performance of the electrocatalysts was evaluated in a H_2 -saturated $0.5 \text{ M H}_2\text{SO}_4$ aqueous solution using a rotating disk electrode. As shown in Fig. 2a, b and Supplementary Figs. 19 and 20, Ru/C shows negligible catalytic activity, much inferior to the case in alkaline media (Supplementary Fig. 19), which is in great part due to the strong HBE on Ru sites.⁴² Interestingly, Pt1-Ru/C exhibits substantially improved HOR activity after decorating Pt single atoms on Ru NCs, with a much higher HOR kinetic current (j_k) and exchange current density (j_0) (Fig. 2b and Supplementary Fig. 20). The catalytic activity initially increases with increasing the density of Pt single atoms until

reaching its maximum (Supplementary Fig. 20), which probably arises from the saturation of Pt single atoms anchored on the Ru NCs.^{43,44} The carbon-supported Pt single atoms (denoted as Pt1/C, see Experimental Section and Supplementary Figs. 21 and 22) is catalytically inactive for the HOR process, suggesting that the residual Pt single atoms deposited on the carbon support are not responsible for the enhanced catalytic performance of Ru NCs. Therefore, these results strongly suggest that the coupling of Ru NCs and Pt single atoms contributes to the remarkable enhancement in catalytic activity. Notably, the catalytic performance of the optimal Pt1-Ru/C is much superior to Pt/C in terms of intrinsic activity and mass activity (Supplementary Fig. 20c, d, 23, and 24). The polarization curves collected at different rotation speeds for the Pt1-Ru/C catalyst are shown in Supplementary Fig. 25, and the corresponding Koutecky–Levich plot shows a linear relationship between $\omega^{-1/2}$ and the inverse of current density at an overpotential of 30 mV. The slope is calculated to be $4.81 \text{ cm}^2 \text{ mA}^{-1} \text{ s}^{-1/2}$, which is very close to the theoretical value ($4.87 \text{ cm}^2 \text{ mA}^{-1} \text{ s}^{-1/2}$) for a two-electron reaction.^{45–47} The HOR stability of the catalysts was evaluated by an accelerated durability test (ADT) as depicted in Supplementary Fig. 26a. After 1000, 3000, and 5000 cyclic voltammetry (CV) cycles, the overpotential at 1 mA cm^{-2} of Pt1-Ru/C increases by only about 1, 2 and 4 mV, respectively, much superior to those of Pt/C (Supplementary Fig. 26b). HAADF-STEM images of Pt1-Ru/C after the ADT indicate no significant changes (Supplementary Fig. 27), demonstrating the robust structural stability. Furthermore, the Pt1-Ru/C catalyst displays almost no decay for 70 h operation at an overpotential of 20 mV (Supplementary Fig. 28). The Pt1-Ru/C catalyst demonstrates outstanding resistance to CO poisoning, as evidenced by the chronoamperometry test at 0.1 V (versus RHE) in $\text{H}_2/1000 \text{ ppm CO}$ -saturated $0.5 \text{ M H}_2\text{SO}_4$ solution (Supplementary Fig. 29), which possibly is

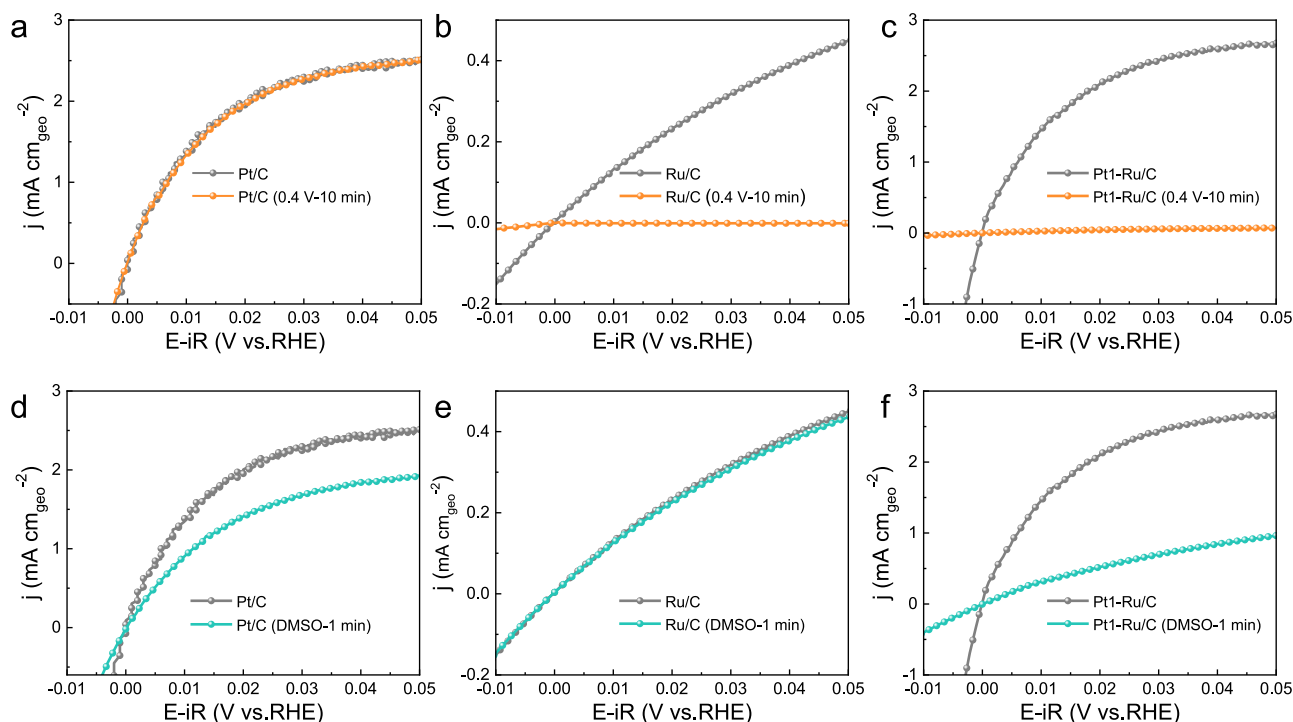


Fig. 3 | Electrochemical experimental evidence for the tandem electrocatalysis mechanism. **a–c** LSV curves before and after passivating at 0.4 V (versus RHE) for 10 min of **a** Pt/C, **b** Ru/C, and **c** Pt1-Ru/C. **d–f** LSV curves before and after immersing in DMSO aqueous solution for 1 min of **d** Pt/C, **e** Ru/C, and **f** Pt1-Ru/C. All LSV curves

were collected at a scan rate of 0.5 mV s^{-1} with 90% iR compensation on a RDE at 1600 rpm. The ohmic resistance ($5 \pm 0.3 \Omega$) for iR compensation was obtained from EIS analysis with a geometric area of 0.19625 cm^2 . Source data are provided as a Source Data file.

attributed to the weakened CO adsorption capability of Ru induced by electron transfer from Ru to Pt.⁴⁸ Additionally, CO-stripping experiments were conducted to assess the CO resistance of Pt1-Ru/C (Supplementary Fig. 30). The Pt1-Ru/C catalyst exhibits a significantly lower onset potential for CO stripping compared with Ru/C and Pt/C catalysts, consistent with its superior CO tolerance.⁴⁹ All CV data were iR-corrected using the ohmic resistance ($5 \pm 0.3 \Omega \text{ cm}^2$) obtained from electrochemical impedance spectroscopy (EIS) analysis and a geometric area of 0.19625 cm^2 . The non-iR-corrected CV data are presented in Supplementary Fig. 20e.

To further evaluate the catalytic performance, the Pt1-Ru/C catalyst was integrated into the anode of the membrane electrode assembly (MEA) for PEMFCs, and the fuel cells with anode PGM loadings of $0.005 \text{ mg}_{\text{PGM}} \text{ cm}^{-2}$ for Pt1-Ru/C and $0.05 \text{ mg}_{\text{Pt}} \text{ cm}^{-2}$ for commercial Pt/C were tested. The maximum power density (P_{max}) of the PEMFC with the Pt1-Ru/C anode catalyst reaches 1.91 W cm^{-2} (Fig. 2c), which is comparable to the state-of-the-art Pt-based anode catalysts (Supplementary Fig. 31a and Supplementary Table 5).^{12,50} The activity normalized by the anode PGM mass at 0.6 V is $520 \text{ A mg}_{\text{PGM}}^{-1}$ under a $\text{H}_2\text{-O}_2$ condition, surpassing other catalyst systems in reported PEMFCs (Supplementary Fig. 31b and Supplementary Table 5). Moreover, as displayed in the mass-specific Tafel plots, the Pt1-Ru/C delivers a high anodic mass activity of $23.12 \text{ A mg}_{\text{PGM}}^{-1}$ at $0.9 \text{ V}_{\text{IR-free}}$, an order of magnitude higher than Pt/C ($2.01 \text{ A mg}_{\text{PGM}}^{-1}$) (Supplementary Fig. 32a). Considering that the price of Ru is approximately 38% of that of Pt (Supplementary Table 6),^{51,52} compared with Pt/C, Pt1-Ru/C exhibits a 95.6% reduction in anode specific power cost (P_{max}) (Supplementary Fig. 32b and Supplementary Table 6). Additionally, Pt1-Ru/C shows inferior ORR catalytic activity, which alleviates the MEA degradation under start/stop conditions (Supplementary Fig. 33).^{53–55} The potential of Pt1-Ru/C for automobile applications is further assessed with air as the cathodic gas feed. The cell achieves a P_{max} of 0.95 W cm^{-2} and a current density of 302 mA cm^{-2} at 0.8 V (Fig. 2d). The durability of the PEMFC with the Pt1-Ru/C anode was further evaluated through

continuous operation at 0.6 V under a $\text{H}_2\text{-air}$ condition for 40 h (Supplementary Fig. 34a), and the polarization and power density plots of the PEMFC were obtained before and after the continuous operation in both $\text{H}_2\text{-O}_2$ and $\text{H}_2\text{-air}$ conditions (Supplementary Fig. 34b, c). The polarization and power density curves of the PEMFC demonstrate minor degradation after stability testing, confirming the stability of the Pt1-Ru/C anode catalyst. Clearly, the Pt1-Ru/C catalyst shows great potential to replace Pt/C, which would significantly reduce the cost of the anode catalyst for PEMFCs.

Mechanism investigation

To elucidate the intrinsic mechanism for the outstanding catalytic activity of Pt1-Ru/C, a series of electrochemical experiments were performed (Fig. 3 and Supplementary Fig. 35). Linear sweep voltammetry (LSV) curves were measured subsequent to passivating Ru/C, Pt1-Ru/C, and commercial Pt/C catalysts at 0.4 V (versus RHE) for 10 min (Note: Ru undergoes oxidation at potentials of over 0.1 V) (Fig. 3a–c).⁵¹ As shown in Fig. 3a, Pt/C is not affected after passivation, while the HOR activity of Ru/C and Pt1-Ru/C vanishes entirely (Fig. 3b, c), indicating that the presence of metallic Ru is critical to catalyze the HOR and individual Pt single atoms are fully inactive. The freshly prepared electrodes coated with the catalysts were immersed in DMSO aqueous solution for 1 min, and were then rinsed in $0.5 \text{ M H}_2\text{SO}_4$ solution for 10 min (see electrochemical testing for details) before conducting the LSV test (Fig. 3d, e). As a soft base, DMSO can coordinate with Pt, which is a soft acid, thereby hindering the adsorption of H^+ on Pt (Fig. 3d–f).⁵⁶ In contrast, Ru, as a borderline acid, forms weaker coordination with DMSO and is effectively removed during the rinsing process, resulting in negligible impact on the performance of Ru/C catalyst (Fig. 3e). As revealed in Fig. 3f, DMSO significantly weakens the HOR activity of the Pt1-Ru/C catalyst, indicating that the Pt sites also play a crucial role besides Ru. On the basis of the aforementioned discussion, it can be concluded that both Ru and Pt sites are indispensable for delivering fast HOR kinetics on Pt1-Ru/C. Accordingly, we

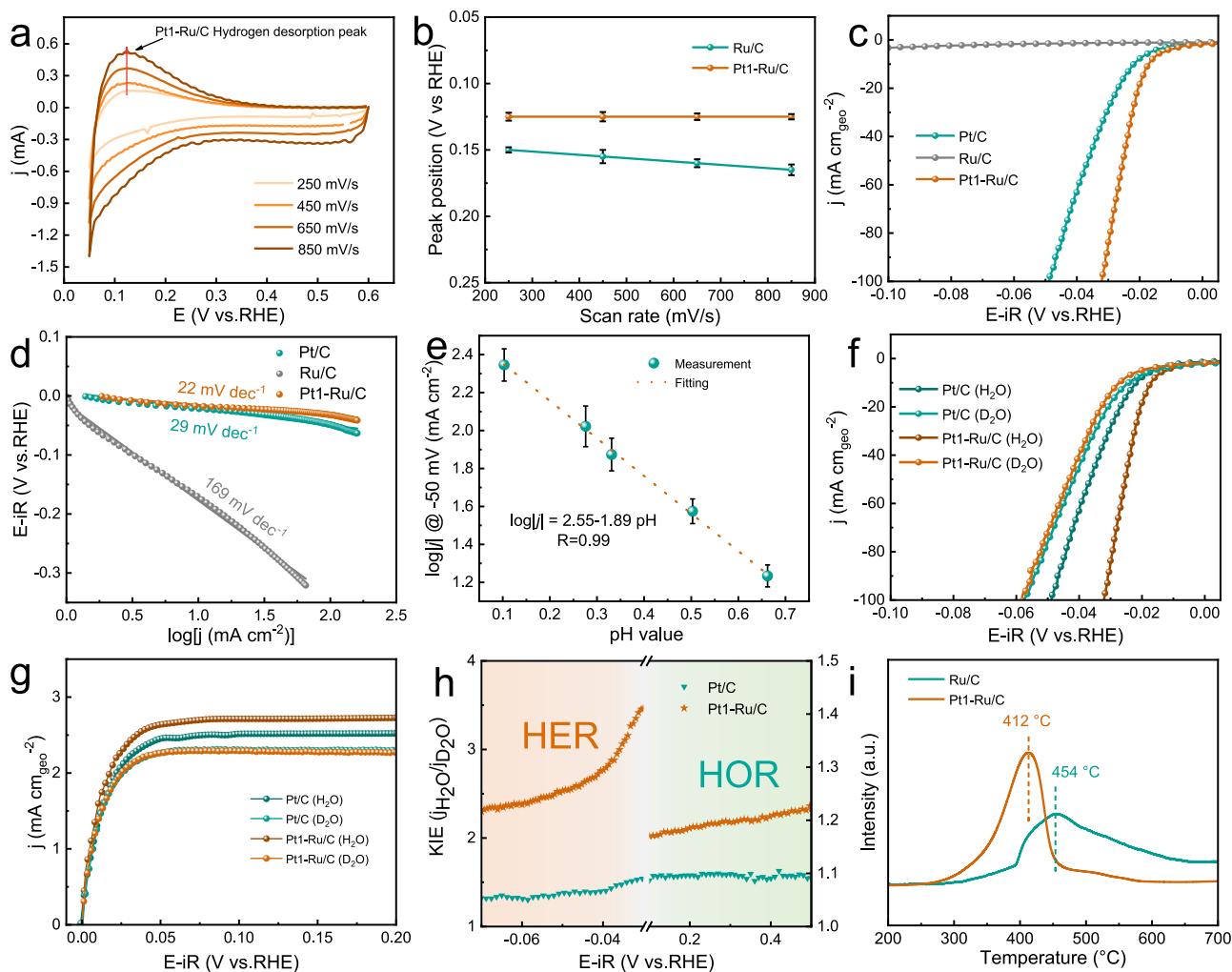


Fig. 4 | Electrochemical experimental evidences for hydrogen spillover. **a** CV of the Pt1-Ru/C catalyst in a N_2 -saturated 0.5 M H_2SO_4 with different scan rates without iR correction. **b** Plots of hydrogen desorption peak position versus scan rates of the Ru/C and Pt1-Ru/C. **c** HER polarization curves and **d** Tafel plots of different catalysts in N_2 -saturated 0.5 M H_2SO_4 with a rotating speed of 1600 rpm. **e** Plots of $\log|j|$ at -0.05 V (RHE) versus pH for Pt1-Ru/C catalyst. **f** HER polarization curves of Pt/C and Pt1-Ru/C catalysts in N_2 -saturated 0.5 M H_2SO_4 aqueous solution and N_2 -saturated 0.5 M D_2SO_4 deuterium oxide (D_2O) solution. **g** HOR polarization curves of Pt/C and

Pt1-Ru/C catalysts in H_2 -saturated 0.5 M H_2SO_4 aqueous solution and H_2 -saturated 0.5 M D_2SO_4 deuterium oxide (D_2O) solution. **h** H/D isotope effect analysis (j_{H_2O}/j_{D_2O} versus potential) for Pt/C and Pt1-Ru/C. **i** H_2 -TPD profiles of Ru/C and Pt1-Ru/C. All LSV curves were collected at a scan rate of 0.5 $mV s^{-1}$ with 90% iR compensation on a RDE at 1600 rpm. The ohmic resistance ($5 \pm 0.3 \Omega$) for iR compensation was obtained from EIS analysis with a geometric area of 0.19625 cm^2 . Source data are provided as a Source Data file. Error bars indicate standard errors obtained from 3 independent replicates.

propose that the whole hydrogen oxidation process might happen via a tandem catalysis mechanism, with hydrogen dissociation and oxidation on Ru and Pt sites, respectively, and hydrogen spillover from Ru to Pt is the key in this process.

The H^* desorption kinetics for metal electrocatalysts could be effectively accelerated by the hydrogen spillover effect, and hence the occurrence of the hydrogen spillover can be verified by analyzing the H^* desorption kinetics.^{57–60} To quantify the H^* desorption kinetics, the CV curves at different scan rates were collected (Fig. 4a and Supplementary Fig. 36), and the H^* desorption peak positions at different scan rates were plotted (Fig. 4b). The pronouncedly reduced slope for Pt1-Ru/C suggests substantially accelerated H^* desorption kinetics and a distinct hydrogen spillover process occurs. Besides, the hydrogen spillover effect can also arise in acidic HER, where H^* is the only reaction intermediate.^{57,58} As depicted in Fig. 4c and Supplementary Fig. 37, the acidic HER performance of Pt1-Ru/C is significantly superior to that of commercial Pt/C. The Tafel slope of Pt1-Ru/C is 22 $mV dec^{-1}$ (Fig. 4d), and the decreased Tafel slope indicates an accelerated H^* adsorption kinetics, which is ascribed to the hydrogen spillover effect.^{57,58,61–63} Additionally, the hydrogen spillover effect is further

verified by the pH-dependent HER experiments (Supplementary Fig. 38). The reaction order of 1.89 for Pt1-Ru/C (Fig. 4e) is similar to the that of the previously reported hydrogen spillover-involved catalysts and close to the theoretical value of 2.^{57,58,61–63} The in situ EIS investigations were further carried out to investigate the hydrogen adsorption kinetics. The recorded Nyquist plots were simulated by a double-parallel equivalent circuit model (Supplementary Figs. 39 and 40, and Supplementary Table 7). The second parallel component R_2 (R_2 represents the hydrogen adsorption resistance) can reflect the hydrogen adsorption behavior on catalyst surface.^{49,57,58,64,65} The hydrogen adsorption kinetics of different catalysts are quantified by plotting $\log R_2$ versus overpotential and calculating the EIS-derived Tafel slopes. As shown in Supplementary Fig. 41, the significantly declined EIS-derived Tafel slope for Pt1-Ru/C indicates an accelerated hydrogen adsorption kinetics, further demonstrating the existence of the hydrogen spillover process.⁵⁸ Furthermore, the H/D kinetic isotope effect (KIE) can reflect the H^* transfer kinetic information of chemical reactions. Generally, the KIE value exceeding 1.5 reveals that the reaction involves the H^* transfer process.^{57,66–69} The KIE experiments in 0.5 M D_2SO_4/D_2O solution were performed to obtain more insights

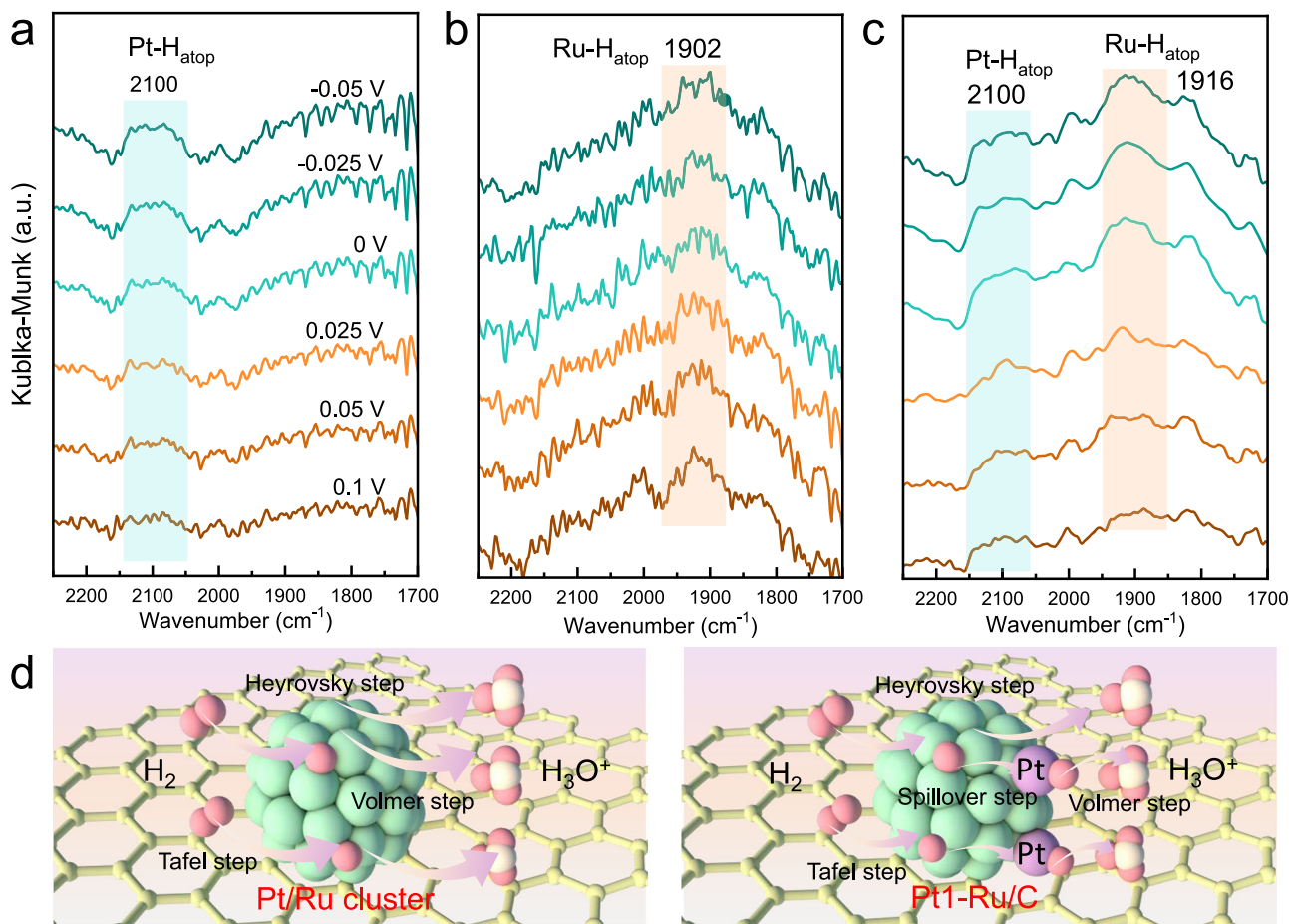


Fig. 5 | Spectroscopic evidence for hydrogen spillover and the schematic diagram for the HOR processes. The in situ synchrotron ATR-FTIR spectra of **a** Pt/C, **b** Ru/C, and **c** Pt1-Ru/C catalysts. **d** Schematic illustration of the traditional HOR and tandem HOR processes, in which the green clusters denote Ru or Pt clusters, the

purple spheres represent Pt atoms, the pink spheres signify H atoms, the white spheres indicate O atoms, and the light green spheres correspond to C atoms. Source data are provided as a Source Data file.

into the hydrogen spillover during the HER (Fig. 4f and Supplementary Fig. 42) and HOR (Fig. 4g and Supplementary Fig. 43) processes. In the HER potential range, the KIE values for both Ru/C and Pt/C are below 1.5 (Supplementary Fig. 44 and Fig. 4h), while those for Pt1-Ru/C range from 2.2 to 3.6 (Fig. 4h), suggesting the participation of deuterium atoms in the hydrogen spillover process that decreases the HER rate accordingly. During the HOR process, H^{*} are generated from the dissociation of H₂, and deuterium atoms in D₂O are excluded from the hydrogen spillover process, which leads to the lack of a significant effect of D₂O on the kinetic current of HOR (Supplementary Fig. 45). However, due to the lower H₂ mass diffusion coefficient in D₂O compared with that in H₂O,⁷⁰ the limiting current of HOR decreases (Fig. 4g and Supplementary Fig. 43). Furthermore, since the mass transfer rate of H^{*} also decreases in D₂O,⁷⁰ the catalysts that exhibit hydrogen spillover behavior will undergo more serious mass transfer limitation in D₂O. At the limiting current potential range (0.1–0.5 V versus RHE), the KIE values for Pt1-Ru/C, Pt/C, and Ru/C are 1.2, 1.1, and 1.1, respectively (Fig. 4h and Supplementary Fig. 46), indicating that the mass transfer on Pt1-Ru/C is restricted more significantly, which provides further evidence for the hydrogen spillover process occurring on Pt1-Ru/C. Hydrogen temperature-programmed desorption (H₂-TPD) tests were conducted to demonstrate the changes in hydrogen desorption capacity. As shown in Fig. 4i, the hydrogen desorption peak temperature of Pt1-Ru/C is lower than that of Ru/C, further confirming that hydrogen spillover greatly facilitates the hydrogen desorption process.⁵⁷

In situ synchrotron Fourier-transform infrared spectroscopy in attenuated total reflection (ATR-FTIR) mode was performed to provide more evidence for the existence of the hydrogen spillover process (Fig. 5a–c and Supplementary Fig. 47). As depicted in Fig. 5a–c, the peak at around 2100 cm⁻¹ corresponds to the atop adsorption of hydrogen on Pt (Pt-H_{atop}),^{71,72} while the peak at around 1900 cm⁻¹ is attributed to the atop adsorption of hydrogen on Ru (Ru-H_{atop}).^{71,73} As the potential increases from -0.05 V to 0.1 V, the Pt-H_{atop} peak of Pt/C gradually disappears along with the continuous hydrogen oxidation and desorption (Fig. 5a), while the Ru-H_{atop} peak of Ru/C shows no noticeable change (Fig. 5b) due to the strong H^{*} adsorption of Ru. In contrast, for Pt1-Ru/C, the adsorption peaks of H^{*} on both Ru and Pt sites become weakened (Fig. 5c) as the potential increases, suggesting that the hydrogen desorption is promoted on Ru sites, which is closely associated with the significant hydrogen spillover from Ru to Pt sites. Therefore, the electrochemical and spectroscopic results strongly evidence that pronounced hydrogen spillover from Ru to Pt occurs during the hydrogen electrocatalysis process, and eventually decouples the acidic HOR on Pt1-Ru/C.

As illustrated in Fig. 5d, the complete decoupled HOR process follows two possible pathways: the Tafel-Spillover-Volmer pathway and the Heyrovsky-Spillover-Volmer pathway. In the Tafel-Spillover-Volmer pathway, H₂ first diffuses and adsorbs onto Ru NCs, and then dissociates into H^{*}. Subsequently, H^{*} spills over to nearby Pt single atoms to form Pt-H^{*}, eventually desorbing from Pt to become H⁺. In contrast, in the Heyrovsky-Spillover-Volmer pathway, half of the H^{*}

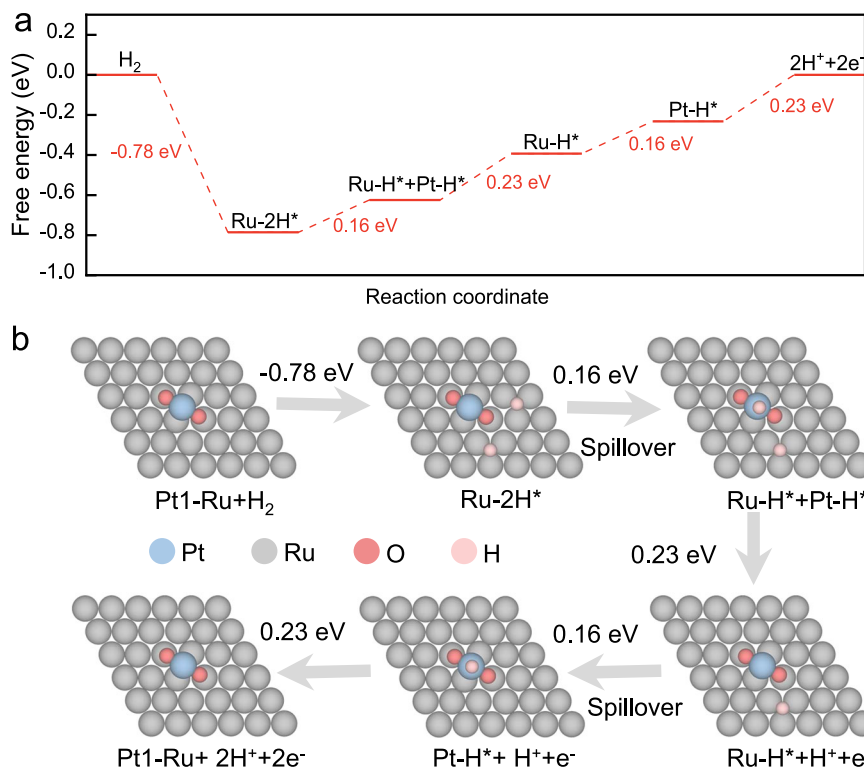


Fig. 6 | Theoretical calculation investigations. **a** Gibbs free energy diagram for HOR on Pt1-Ru. **b** Pt1-Ru models and schematic diagrams of the hydrogen spillover process as well as the corresponding free energy of each step. Source data are provided as a Source Data file.

adsorbed on Ru desorbs directly as H^+ , while the other half spills over to Pt single atoms and desorbs as H^+ .

DFT calculations were carried out to further support the thermodynamic advantages of decoupling HOR on a tandem Pt1-Ru/C electrocatalyst (Fig. 6, Supplementary Figs. 48 and 49, and Supplementary Data 1). The unrelated atoms are removed for a clear demonstration. The adsorption and dissociation of H_2 on Ru and Pt sites are thermodynamically spontaneous. The free energy for the direct desorption of H^* from Ru and Pt sites are 0.44 and 0.31 eV, respectively (Supplementary Figs. 48 and 49). In contrast, the free energy for the hydrogen spillover from Ru to Pt single atoms and desorption from Pt single atoms are 0.16 and 0.23 eV, respectively (Fig. 6a, b). This result supports that the decoupled HOR enabled by the hydrogen spillover effect not only reduces the desorption free energy of H^* at Ru sites but also lowers the energy barrier of the rate-determining Volmer step, which explains why the Pt1-Ru/C catalyst exhibits superior catalytic performance to Ru/C and Pt/C.

To further validate the universal feasibility of decoupling HOR toward faster reaction kinetics, a variety of catalysts with similar structures were designed as the potential tandem electrocatalysts (Supplementary Figs. 50–52). Pd single atoms and Ir single atoms were firstly selected to replace Pt single atoms. As revealed in Supplementary Fig. 50, the coupling of Ru NCs with Pd single atoms has almost no promotion effect on the HOR kinetics, whereas the presence of Ir single atoms significantly enhances the HOR performance. The possible reason is that the robust H^* adsorption capabilities of both Ru and Pd make it difficult for H^* to desorb quickly, while Ir single atoms with weaker H^* adsorption ability can enable the decoupling of HOR through the hydrogen spillover effect, which is similar to the case of Pt1-Ru/C. Pd and Ni with strong H^* adsorption capabilities were used to replace Ru NCs. As shown in Supplementary Figs. 51 and 52, the incorporation of Pt single atoms can effectively enhance the HOR performance of Pd and Ni as well. The above results demonstrate the

feasibility and versatility of the concept of decoupling HOR on tandem catalysts toward faster reaction kinetics.

Discussion

We propose a concept of tandem electrocatalysis to decouple the HOR process toward faster reaction kinetics, and develop a highly efficient Ru-based tandem HOR electrocatalyst, with Ru NCs decorated with Pt single atoms. The electrochemical experiments along with the in situ infrared spectroscopy evidence the successful decoupling of the HOR and the hydrogen spillover from Ru to Pt sites. The theoretical calculations demonstrate that the decoupling of HOR reduces the free energy of the rate-determining Volmer step, thereby improving the catalytic performance. The fuel cell with ultralow loading of Pt1-Ru/C anode catalyst ($5 \mu\text{g}_{\text{PGM}} \text{cm}^{-2}$) achieves a peak power density of 1.91 W cm^{-2} and establishes a groundbreaking anodic mass activity of $23.12 \text{ A mg}^{-1}_{\text{PGM}}$ at $0.9 \text{ V}_{\text{ir-free}}$. The strategy of decoupling HOR on a tandem catalyst not only contributes to developing efficient and economical anode catalysts for PEMFCs but also provides more guidance for designing advanced electrocatalysts for a broad range of catalytic reactions.

Methods

Chemicals

Carbon black (S.A. $75 \text{ m}^2 \text{ g}^{-1}$, CAS: 1333-86-4) was purchased from Alfa Aesar. $\text{RuCl}_3 \cdot 3\text{H}_2\text{O}$, H_2PtCl_6 , K_2PdCl_6 , IrCl_3 , Nafion 117 solution, and 20 wt% Pt/C (activated carbon support) were purchased from Sigma-Aldrich (Australia). Acetone and HNO_3 were purchased from Sino-pharm Chemical Reagent Co., Ltd. Ethanol (EtOH, 99.9%) was purchased from Shanghai Aladdin Biochemical Technology Co., Ltd. Ultrapure deionized water (DIW , $18 \text{ M}\Omega \text{ cm}^{-1}$) was used in all the experiments. Dimethyl sulfoxide (DMSO, > 99.5%) was purchased from Macklin. All the chemicals were used as received without further purification.

Synthesis of Ru/C, Pd/C, and Ni/C

First, 500 mg carbon black was dispersed in 30 mL of concentrated HNO₃ solution (8 mol/L) and stirred at 80 °C for 12 h to enhance the hydrophilicity of the carbon black support. The HNO₃-functionalized carbon black was collected, washed several times with DIW and ethanol, and subsequently dried in a vacuum oven at 80 °C for 12 h.

Ru/C was prepared a facile impregnation method. 30 mg of functionalized carbon black was mixed with 0.25 mL of 0.1 M RuCl₃ solution and stirred at room temperature (25 °C) for 12 h. The sample was then centrifuged and washed several times with DIW and ethanol, followed by drying in a vacuum oven at 80 °C for 12 h. Finally, the sample was annealed at 300 °C for 3 h in 10% H₂/Ar to eventually obtain Ru/C.

Pd/C and Ni/C were prepared via the same process to Ru/C except for replacing the RuCl₃ solution with H₂PdCl₆ and NiCl₂ solution, respectively.

Synthesis of Pt1-Ru/C, Pd1-Ru/C, Ir1-Ru/C, Pt1-Pd/C, and Pt1-Ni/C

20 mg Ru/C catalyst was thoroughly mixed with 60 μL 0.01 M H₂PtCl₆ solution in 20 mL of DIW. The mixture was stirred at 1500 rpm for 30 min, followed by centrifugation. The resulting material was washed several times with DIW and ethanol, and then dried in a vacuum oven at 80 °C for 12 h to obtain the Pt1-Ru/C catalyst. The control samples of Pt1-Ru/C-0.5 and Pt1-Ru/C-2 were synthesized via the same method, with the addition of 30 and 120 μL of 0.01 M H₂PtCl₆ solution, respectively.

Pd1-Ru/C and Ir1-Ru/C were synthesized via the same method as Pt1-Ru/C, except that the H₂PtCl₆ solution was replaced by K₂PdCl₆ and IrCl₃ solution, respectively.

Pt1-Pd/C and Pt1-Ir/C were synthesized via the same method as Pt1-Ru/C, except that Ru/C was replaced by Pd/C and Ir/C, respectively.

Synthesis of Pt1/C

20 mg of functionalized carbon black was mixed with 60 μL of 0.01 M H₂PtCl₆ solution in 20 mL of DIW. The mixture was stirred at 1500 rpm for 30 min, followed by centrifugation. The resulting material was washed several times with DIW and ethanol, and then dried in a vacuum oven at 80 °C for 12 h.

Characterizations

XRD patterns were recorded on a RigakuDmax-rc X-ray diffractometer with Cu Kα (λ = 1.5418 Å) radiation. Transmission electron microscopy (TEM) and HRTEM were acquired with a FEI Tecnai G2 F20 S-TWIN electron microscope operating at 200 kV. Atomic solution HAADF-STEM images and energy-dispersive EDS were collected on an ARM-ARM200F electron microscope operating at 200 kV. X-ray photoelectron spectroscopy was conducted on an ESCALAB 250Xi. Hard X-ray absorption spectra at Pt L₃-edge ($E_0 = 11564$ eV) and Ru K-edge ($E_0 = 22117$ eV) were performed at beamline BL20U and BL11B of Shanghai Synchrotron Radiation Facility operated at 3.5 GeV under “top-up” mode with a constant current of 220 mA, respectively. The Pt L₃-edge spectra were recorded under fluorescence mode with a Lytle chamber. The white light was monochromatized by a Si (111) double-crystal monochromator. The Ru K-edge spectra were recorded under transmission mode. The white light was monochromatized by a Si (311) double-crystal monochromator. The data processing was conducted using Demeter software.³⁹ Athena and Artemis codes were used to extract and fit data. For the XANES part, background subtraction and normalization procedures processed the experimental absorption coefficients as a function of energies μ(E). The spectra were corrected according to the first and largest peak of the first derivative of XANES, then normalized and background removed with a k^3 -weighting and a R_{bkg} value of 1.0. The normalized EXAFS spectra were obtained by subtracting the post-edge background from the overall absorption and then normalizing the edge-jump step. For the

EXAFS part, the Fourier-transformed data were fitted in R space. The passive electron factors, S_0^2 , were determined by fitting the experimental Pt-foil and Ru-foil data, and then fixed for further analysis of the measured samples. The parameters described by the local structure environment including coordination numbers (N), bond distance (R), and Debye-Waller (σ^2) factor around the absorbed atoms were allowed to vary during the fit process. The quantitative structural parameters were obtained by a least-squares curve parameter fitting for the EXAFS spectra by ARTEMIS module. The CCWT methodology deconvolved the data.⁷⁴ The Cauchy wavelet was chosen as the basis mother wavelet and the Cauchy order was set as 200 for a better analysis.

Electrochemical Tests

Electrochemical tests were carried out in H₂-saturated 0.5 M H₂SO₄ aqueous solution for the HOR and in N₂-saturated 0.5 M H₂SO₄ aqueous solution for the HER at a scan rate of 0.5 mV s⁻¹ with 90% iR compensation on a rotating disk electrode (RDE) at 1600 rpm. The electrolyte used in this work was a commercial 0.5 M H₂SO₄ solution, which was stored at room temperature. All potentials were iR-corrected based on the resistance values obtained from EIS conducted at open-circuit potential (OCP) over a frequency range of 100 kHz–10 Hz. The resistance (R) was extracted from the high-frequency intercept on the real axis of the Nyquist plot and used in the correction formula: $E_{\text{corrected}} = E_{\text{measured}} - 0.9 \times iR$. A standard three-electrode cell system coupled with electrochemical station (Chi 760E) was used for evaluating the electrocatalytic performance. An Ag/AgCl electrode was used as the reference electrode, which was calibrated with a reversible hydrogen electrode (RHE). In 0.5 M H₂SO₄, a three-electrode system (H₂-saturated Pt as working electrode/RHE, Ag/AgCl as reference electrode, and Pt-foil as counter electrode) is established under H₂ purging (≥30 min). The OCP is measured via CV (1 mV s⁻¹), with the anodic/cathodic peak crossover potential defining the Ag/AgCl potential versus RHE. Post-use, rinse with DIW and store in 3 M KCl to prevent sulfate contamination. A Pt mesh electrode and a graphite rod were used as the counter electrode for the HOR and HER, respectively. The preparation process of the working electrode involves dropping different volumes of catalyst ink onto a glassy carbon electrode, where the catalyst loading is 12 μg_{PGM} cm⁻² for Pt/C working electrodes, and 2 μg_{PGM} cm⁻² for Ru/C and Pt1-Ru/C working electrodes. The effective area of the working electrode is 0.19625 cm². To prepare the catalyst inks, 2 mg catalysts were dispersed in a mixed solution containing 5 μL 5% Nafion solution and 495 μL ethanol, and were treated with ultrasonication for 2 h. The working electrode was first cycled between -0.1 ~ 0.6 V (versus RHE) at a scan rate of 30 mV s⁻¹ for 5 CV cycles for the HOR. After that, the linear sweep voltammetry (LSV) curve was recorded at a scan rate of 1.0 mV s⁻¹ at a rotation speed of 1600 rpm to evaluate the catalytic activity. The resistance to CO poisoning of different catalysts was evaluated via chronoamperometry test at 0.1 V (versus RHE) in H₂/1000 ppm CO-saturated (0.5 M) H₂SO₄ solution.

The treatment of the electrode in DMSO aqueous solution (50 vol%) is conducted as follows: the electrode surface was immersed in 20 mL of DMSO aqueous solution for 1 min, then was quickly removed and rotated in 200 mL of 0.5 M H₂SO₄ for 10 min to wash off any residual organic substances on the surface (incomplete cleaning of organic substances can hinder the diffusion of hydrogen between the solution and the electrode surface).

When conducting the CO stripping experiments, the CO adsorption was firstly performed with amperometric i-t test at 0.05 V (versus RHE) for 10 min in a CO-saturated 0.1 M KOH aqueous solution. Then the electrode was transferred into a N₂-saturated 0.1 M KOH aqueous solution. The CO stripping current was obtained by CV in the potential range of 0–1.1 V versus RHE at a scan rate of 50 mV s⁻¹.

The EIS was measured at different overpotentials in H₂-saturated 0.5 M H₂SO₄ solution with an amplitude voltage of 5 mV in a frequency range of 100 kHz–0.1 kHz.

As the HOR is dominated by the mass transport of H₂ to the electrode surface due to its limited solubility in the electrolyte (<1 mmol L⁻¹ at room temperature (25 °C)), the limiting current density was calculated based on the Levich equation:⁷⁵

$$j_L = 0.62nFD^{2/3}\nu^{-1/6}c_0\omega^{1/2} = Bc_0\omega^{1/2} \quad (1)$$

where j_L is the limiting current, n is the number of electrons transferred in the HOR ($n = 2$), F is the Faraday constant (96,485 A s mol⁻¹), D is the diffusivity of H₂ in the electrolyte, ν is the kinematic viscosity of the electrolyte, c_0 is the solubility of H₂ in electrolyte and ω is the rotation speed. B represents $0.62nFD^{2/3}\nu^{-1/6}$.

The kinetic current (j_k) was calculated based on the Koutecky–Levich equation:

$$\frac{1}{j} = \frac{1}{j_k} + \frac{1}{j_D} \quad (2)$$

where j stands for the measured current and j_D represents the diffusion current. j_D can be obtained based on Nernstian diffusion overpotential equation.

$$j_D = j_L \left(1 - e^{-\frac{2F\eta}{RT}}\right) \quad (3)$$

The specific exchange current density (j_0) was obtained by calculating the with Butler–Volmer equation:

$$j_k = j_0 \left[e^{\frac{\alpha F\eta}{RT}} - e^{-\frac{(1-\alpha)F\eta}{RT}} \right] \quad (4)$$

where α is the charge transfer coefficient, R is the universal gas constant (8.314 J mol⁻¹ K⁻¹), and T is the temperature (K), α and j_0 were set as variables. This formula, when Taylor expanded to the first order at zero, transforms into:

$$j_k = j_0 \frac{F}{RT} \eta \quad (5)$$

Therefore, near the zero point (<5 mV), the kinetic current is linearly related to the potential. j_0 can be calculated by fitting the slope of the linear region, and the equation is:

$$j_0 = \frac{RT}{F} \frac{dj_k}{d\eta} \quad (6)$$

Computational details

In this work, all first-principle calculations were performed using DFT implemented in the Vienna Ab initio Simulation Package developed by Hafner's group.^{76,77} The projector augmented wave pseudo potentials with the Perdew–Burke–Ernzerhof functional were used. The Brillouin zone gamma point was sampled using a 3 × 3 × 1 Monkhorst–Pack k-point grid. The cut-off energy was set to 500 eV, with a total energy of 10⁻⁵ eV and a force of 0.02 eV/Å per atom, to optimize the structure and perform the self-consistent calculation. The Gibbs free energy was calculated as $\Delta G = \Delta E + \Delta ZPE - T\Delta S$, where ΔE denotes the electron energy; ΔZPE , the zero-point correction energy; T , the reaction temperature; and ΔS , the entropy change, which was determined by using a standard vibrational correction for entropy. In terms of model construction, we chose to expand the single crystal cell and simulated the Ru (001) crystal plane to investigate H adsorption on surface. Among

them, Pt atoms were loaded onto the interstitial sites of Ru to construct Ru–Pt catalysts.

MEA preparation and PEMFC tests

The catalyst inks were made by dispersing the catalysts in n-propanol to water (1:1) solvent mixture with D72-25BS[®] perfluorosulfonic acid ionomer with an equivalent weight of 720 g mol⁻¹ at an ionomer to carbon ratio of 0.8, by sonication for 2 h. The Pt loading was set at 0.1 mg cm⁻². The catalyst-coated-membrane (CCM) was with an active area of 5 cm² was prepared on Nafion membrane (GORE, -12 μm) with an ultrasonic spray (ExactaCoat FC, Sono-Tek Corporation). The fabricated CCM was dried to completely evaporate the solvents to obtain the MEA. For H₂–O₂ and H₂–Air single cell tests, the commercial 30 wt% Pt/C (TEC10E30E, TTK) was used on the cathode with a Pt loading of 0.1 mg cm⁻², and the Pt1–Ru/C was used on anode with a PGM loading of 5 μg cm⁻². For comparison, MEA with 30 wt% Pt/C (TEC10E30E, TTK) anode with a Pt loading of 0.05 mg cm⁻² was also tested. A fuel cell test station (Scribner 850e) was used for single cell tests. The anode/cathode humidifier temperatures and cell temperature were consistently maintained at 80 °C. The absolute pressure for both the anode and cathode was set at 250 kPa, with 100% relative humidity (RH), and the flow rates of H₂, O₂, and air were 1.0, 2.0, and 2.0 L min⁻¹, respectively, unless otherwise stated.

Data availability

The data supporting the findings of this study are available within the paper and its Supplementary Information files. Data is available from the corresponding authors on request. Source data are provided with this paper.

References

- Zhang, G. et al. Porous flow field for next-generation proton exchange membrane fuel cells: materials, characterization, design, and challenges. *Chem. Rev.* **123**, 989–1039 (2023).
- Tang, M., Zhang, S. & Chen, S. Pt utilization in proton exchange membrane fuel cells: structure impacting factors and mechanistic insights. *Chem. Soc. Rev.* **51**, 1529–1546 (2022).
- Chong, L. et al. Ultralow-loading platinum-cobalt fuel cell catalysts derived from imidazolate frameworks. *Science* **362**, 1276–1281 (2018).
- Debe, M. K. Electrocatalyst approaches and challenges for automotive fuel cells. *Nature* **486**, 43–51 (2012).
- Wang, J. et al. Poly(aryl piperidinium) membranes and ionomers for hydroxide exchange membrane fuel cells. *Nat. Energy* **4**, 392–398 (2019).
- Wang, Y., Pang, Y., Xu, H., Martinez, A. & Chen, K. S. PEM Fuel cell and electrolysis cell technologies and hydrogen infrastructure development—a review. *Energy Environ. Sci.* **15**, 2288–2328 (2022).
- Scofield, M. E., Liu, H. & Wong, S. S. A concise guide to sustainable PEMFCs: recent advances in improving both oxygen reduction catalysts and proton exchange membranes. *Chem. Soc. Rev.* **44**, 5836–5860 (2015).
- Jacobson, M. Z., Colella, W. G. & Golden, D. M. Cleaning the air and improving health with hydrogen fuel-cell vehicles. *Science* **308**, 1901–1905 (2005).
- Yang, T. et al. High density iridium synergistic sites boosting CO-tolerate performance for PEMFC anode. *eScience* **4**, 100230 (2024).
- Ma, M. et al. Activation methods and underlying performance boosting mechanisms within fuel cell catalyst layer. *eScience* **4**, 100254 (2024).
- Han, C. et al. Metal–support interaction in single-atom electrocatalysts: a perspective of metal oxide supports. *eScience* **4**, 100269 (2024).
- Wang, Q. et al. Atomic metal–non-metal catalytic pair drives efficient hydrogen oxidation catalysis in fuel cells. *Nat. Catal.* **6**, 916–926 (2023).

13. Hsieh, Y.-C. et al. Ordered bilayer ruthenium–platinum core-shell nanoparticles as carbon monoxide-tolerant fuel cell catalysts. *Nat. Commun.* **4**, 2466 (2013).
14. Gao, R. et al. Pt/Fe₂O₃ with Pt–Fe pair sites as a catalyst for oxygen reduction with ultralow Pt loading. *Nat. Energy* **6**, 614–623 (2021).
15. Wan, X. et al. Fe–N–C electrocatalyst with dense active sites and efficient mass transport for high-performance proton exchange membrane fuel cells. *Nat. Catal.* **2**, 259–268 (2019).
16. Gasteiger, H. A. & Marković, N. M. Just a dream-or future reality?. *Science* **324**, 48–49 (2009).
17. Greeley, J. et al. Alloys of platinum and early transition metals as oxygen reduction electrocatalysts. *Nat. Chem.* **1**, 552–556 (2009).
18. Luo, S. et al. Elevated water oxidation by cation leaching enabled tunable surface reconstruction. *Angew. Chem. Int. Ed.* **63**, e202402184 (2024).
19. Wang, Y. et al. Fundamentals, materials, and machine learning of polymer electrolyte membrane fuel cell technology. *Energy AI* **1**, 100014 (2020).
20. Yang, C.-L. et al. Sulfur-anchoring synthesis of platinum inter-metallic nanoparticle catalysts for fuel cells. *Science* **374**, 459–464 (2021).
21. Kodama, K., Nagai, T., Kuwaki, A., Jinnouchi, R. & Morimoto, Y. Challenges in applying highly active Pt-based nanostructured catalysts for oxygen reduction reactions to fuel cell vehicles. *Nat. Nanotechnol.* **16**, 140–147 (2021).
22. Dai, L., Xue, Y., Qu, L., Choi, H.-J. & Baek, J.-B. Metal-free catalysts for oxygen reduction reaction. *Chem. Rev.* **115**, 4823–4892 (2015).
23. Rong, C., Dastafkan, K., Wang, Y. & Zhao, C. Breaking the activity and stability bottlenecks of electrocatalysts for oxygen evolution reactions in acids. *Adv. Mater.* **35**, 2211884 (2023).
24. Zheng, L. et al. Assembling molybdenum-doped platinum clusters into a coral-like nanostructure for highly enhanced oxygen reduction. *eScience* **4**, 100187 (2024).
25. Wang, X., Yu, M. & Feng, X. Electronic structure regulation of noble metal-free materials toward alkaline oxygen electrocatalysis. *eScience* **3**, 100141 (2023).
26. Elvington, M. C. et al. Highly active oxygen reduction electrocatalysts derived from an iron-porphyrin framework. *PRX Energy* **2**, 043008 (2023).
27. Zhou, Y. et al. Lattice-confined Ru clusters with high CO tolerance and activity for the hydrogen oxidation reaction. *Nat. Catal.* **3**, 454–462 (2020).
28. Mehmood, A. et al. High loading of single atomic iron sites in Fe–NC oxygen reduction catalysts for proton exchange membrane fuel cells. *Nat. Catal.* **5**, 311–323 (2022).
29. Xiao, F. et al. Atomically dispersed Pt and Fe sites and Pt–Fe nanoparticles for durable proton exchange membrane fuel cells. *Nat. Catal.* **5**, 503–512 (2022).
30. Xie, X. et al. Performance enhancement and degradation mechanism identification of a single-atom Co–N–C catalyst for proton exchange membrane fuel cells. *Nat. Catal.* **3**, 1044–1054 (2020).
31. Xue, L. et al. Zigzag carbon as efficient and stable oxygen reduction electrocatalyst for proton exchange membrane fuel cells. *Nat. Commun.* **9**, 3819 (2018).
32. Zhang, K. et al. Spin-mediated promotion of Co catalysts for ammonia synthesis. *Science* **383**, 1357–1363 (2024).
33. Quaino, P., Juarez, F., Santos, E. & Schmickler, W. Volcano plots in hydrogen electrocatalysis – uses and abuses. *Beilstein J. Nanotechnol.* **5**, 846–854 (2014).
34. Shen, G. et al. Multi-functional anodes boost the transient power and durability of proton exchange membrane fuel cells. *Nat. Commun.* **11**, 1191 (2020).
35. Jiao, K. et al. Designing the next generation of proton-exchange membrane fuel cells. *Nature* **595**, 361–369 (2021).
36. Yang, F. et al. Sub-3 nm Pt@Ru toward outstanding hydrogen oxidation reaction performance in alkaline media. *J. Am. Chem. Soc.* **145**, 27500–27511 (2023).
37. Mahmood, J. et al. An efficient and pH-universal ruthenium-based catalyst for the hydrogen evolution reaction. *Nat. Nanotechnol.* **12**, 441–446 (2017).
38. A. T. K. Tables of standard electrode potentials: by G. Milazzo and S. Caroli, John Wiley, Chichester and New York, 1978, pp. xvi +421. *J. Mol. Struct.* **54**, 307–308 (1979).
39. Ravel, B. & Newville, M. ATHENA, ARTEMIS, HEPHAESTUS: data analysis for X-ray absorption spectroscopy using IFEFFIT. *J. Synchrotron Radiat.* **12**, 537–541 (2005).
40. Guo, W. et al. Strong metal-support interaction triggered by molten salts. *Angew. Chem. Int. Ed.* **64**, e202414516 (2025).
41. Wang, J. et al. Pt single atoms coupled with Ru nanoclusters enable robust hydrogen oxidation for high-performance anion exchange membrane fuel cells. *Nano Res.* **17**, 6147–6156 (2024).
42. Cai, C. et al. Optimizing hydrogen binding on Ru sites with RuCo alloy nanosheets for efficient alkaline hydrogen evolution. *Angew. Chem. Int. Ed.* **61**, e202113664 (2022).
43. Jin, H., Song, W. & Cao, C. An overview of metal density effects in single-atom catalysts for thermal catalysis. *ACS Catal.* **13**, 15126–15142 (2023).
44. Chang, J. et al. Synthesis of ultrahigh-metal-density single-atom catalysts via metal sulfide-mediated atomic trapping. *Nat. Synth.* **3**, 1427–1438 (2024).
45. Zhuang, Z. et al. Nickel supported on nitrogen-doped carbon nanotubes as hydrogen oxidation reaction catalyst in alkaline electrolyte. *Nat. Commun.* **7**, 10141 (2016).
46. Zhang, B. et al. Lattice-confined Ir Clusters on Pd nanosheets with charge redistribution for the hydrogen oxidation reaction under alkaline conditions. *Adv. Mater.* **33**, 2105400 (2021).
47. Song, F. et al. Interfacial nickel nitride and nickel boosts both electrocatalytic hydrogen evolution and oxidation reactions. *Nat. Commun.* **9**, 4531 (2018).
48. Chen, D.-J. & Tong, Y. J. Irrelevance of carbon monoxide poisoning in the methanol oxidation reaction on a PtRu electrocatalyst. *Angew. Chem. Int. Ed.* **54**, 9394–9398 (2015).
49. Zhang, B. et al. A strongly coupled Ru–CrO_x cluster–cluster heterostructure for efficient alkaline hydrogen electrocatalysis. *Nat. Catal.* **7**, 441–451 (2024).
50. Cao, F. et al. Advances in low Pt loading membrane electrode assembly for proton exchange membrane fuel cells. *Molecules* **28**, 773 (2023).
51. Zhang, X. et al. Toward the fast and durable alkaline hydrogen oxidation reaction on ruthenium. *Energy Environ. Sci.* **15**, 4511–4526 (2022).
52. Yang, J., Zhu, C. & Wang, D. A Simple organo-electrocatalysis system for the chlor-related industry. *Angew. Chem. Int. Ed.* **63**, e202406883 (2024).
53. Yu, Y. et al. A review on performance degradation of proton exchange membrane fuel cells during startup and shutdown processes: causes, consequences, and mitigation strategies. *J. Power Sources* **205**, 10–23 (2012).
54. Reiser, C. A. et al. A reverse-current decay mechanism for fuel cells. *Electrochem. Solid-State Lett.* **8**, A273 (2005).
55. U. S. DOE. DOE technical targets for polymer electrolyte membrane fuel cell components, <https://www.energy.gov/eere/fuelcells/doe-technical-targets-polymer-electrolyte-membrane-fuel-cell-components> (2017).
56. Han, Y., Huynh, H. V. & Tan, G. K. Mono- vs Bis(carbene) complexes: a detailed study on platinum(II)–benzimidazol-2-ylidenes. *Organometallics* **26**, 4612–4617 (2007).

57. Dai, J. et al. Hydrogen spillover in complex oxide multifunctional sites improves acidic hydrogen evolution electrocatalysis. *Nat. Commun.* **13**, 1189 (2022).
58. Li, J. et al. A fundamental viewpoint on the hydrogen spillover phenomenon of electrocatalytic hydrogen evolution. *Nat. Commun.* **12**, 3502 (2021).
59. Park, J. et al. Investigation of the support effect in atomically dispersed Pt on WO_{3-x} for utilization of Pt in the hydrogen evolution reaction. *Angew. Chem. Int. Ed.* **58**, 16038–16042 (2019).
60. Zhan, D., Velmurugan, J. & Mirkin, M. V. Adsorption/desorption of hydrogen on Pt nanoelectrodes: evidence of surface diffusion and spillover. *J. Am. Chem. Soc.* **131**, 14756–14760 (2009).
61. Cheng, Y. et al. Rh-MoS₂ nanocomposite catalysts with Pt-like activity for hydrogen evolution reaction. *Adv. Funct. Mater.* **27**, 1700359 (2017).
62. Sheng, M. et al. Approaching the volcano top: Iridium/Silicon Nanocomposites as efficient electrocatalysts for the hydrogen evolution reaction. *ACS Nano* **13**, 2786–2794 (2019).
63. Zhu, L. et al. A rhodium/silicon co-electrocatalyst design concept to surpass platinum hydrogen evolution activity at high overpotentials. *Nat. Commun.* **7**, 12272 (2016).
64. Zhang, B. et al. Atomically dispersed chromium coordinated with hydroxyl clusters enabling efficient hydrogen oxidation on ruthenium. *Nat. Commun.* **13**, 5894 (2022).
65. Lazanas, A. C. & Prodromidis, M. I. Electrochemical impedance spectroscopy—A tutorial. *ACS Meas. Sci. Au.* **3**, 162–193 (2023).
66. Li, W. et al. A bio-inspired coordination polymer as outstanding water oxidation catalyst via second coordination sphere engineering. *Nat. Commun.* **10**, 5074 (2019).
67. Coggins, M. K., Zhang, M.-T., Chen, Z., Song, N. & Meyer, T. J. Single-site copper(II) water oxidation electrocatalysis: rate enhancements with HPO_4^{2-} as a proton acceptor at pH 8. *Angew. Chem. Int. Ed.* **53**, 12226–12230 (2014).
68. Lewandowska-Andralojc, A. et al. Kinetic and mechanistic studies of carbon-to-metal hydrogen atom transfer involving Os-centered radicals: evidence for tunneling. *J. Am. Chem. Soc.* **136**, 3572–3578 (2014).
69. Li, H., Xie, F. & Zhang, M.-T. Metal-free electrocatalyst for water oxidation initiated by hydrogen atom transfer. *ACS Catal.* **11**, 68–73 (2021).
70. Cussler, E. L. *Diffusion: Mass Transfer in Fluid Systems* (Cambridge University Press, 2009).
71. Zhu, S. et al. The role of ruthenium in improving the kinetics of hydrogen oxidation and evolution reactions of platinum. *Nat. Catal.* **4**, 711–718 (2021).
72. Zhu, S., Qin, X., Yao, Y. & Shao, M. pH-dependent hydrogen and water binding energies on platinum surfaces as directly probed through surface-enhanced infrared absorption spectroscopy. *J. Am. Chem. Soc.* **142**, 8748–8754 (2020).
73. Kubota, J. & Aika, K.-i. FTIR Spectra of terminal and bridged hydrogen atoms adsorbed on ruthenium metal particles dispersed on magnesium oxide. *J. Chem. Soc. Chem. Commun.* **8**, 661–662 (1992).
74. Muñoz, M., Argoul, P. & Farges, F. Continuous Cauchy wavelet transform analyses of EXAFS spectra: a qualitative approach. *Am. Miner.* **88**, 694–700 (2003).
75. Sheng, W. et al. Correlating hydrogen oxidation and evolution activity on platinum at different pH with measured hydrogen binding energy. *Nat. Commun.* **6**, 5848 (2015).
76. Kresse, G. & Furthmüller, J. Efficiency of ab-initio total energy calculations for metals and semiconductors using a plane-wave basis set. *Comput. Mater. Sci.* **6**, 15–50 (1996).
77. Segall, M. D. et al. First-principles simulation: ideas, illustrations and the CASTEP code. *J. Phys.: Condens. Matter* **14**, 2717 (2002).

Acknowledgements

This work was financially supported by the National Natural Science Foundation of China (grant nos. 52171224 (W.S.) and 9226119 (W.S.)). The authors thank beamline BL11B, BL14W1, and BL20U of the Shanghai Synchrotron Radiation Facility (SSRF) for providing the XAFS beamtime, and the staff at Photoemission End-station (BL10B) and the Infrared spectroscopy and micro spectroscopy beamline (BL01B) in the National Synchrotron Radiation Laboratory (NSRL) for their support in XAFS and in situ synchrotron ATR-FTIR measurements. We acknowledge the help of Mr. Yike Ye from Nanyang Technological University and Mr. Han Su from Zhejiang University in DFT calculations.

Author contributions

W.S. conceived the idea. W.G. carried out the materials synthesis, characterization, and performance measurements, analyzed the data, and prepared the manuscript draft. Z.S., D.X., Z.Z., and H.L. conducted the PEMFC tests. B.Z., M.G., Y.L., and H.P. participated in the data analysis and discussion. W.S., W.G., and G.Z. revised the manuscript with input from all authors.

Competing interests

The authors declare no competing interests.

Additional information

Supplementary information The online version contains supplementary material available at <https://doi.org/10.1038/s41467-025-62160-8>.

Correspondence and requests for materials should be addressed to Wenping Sun.

Peer review information *Nature Communications* thanks Deli Wang, Shuifen Xie, and the other, anonymous, reviewer(s) for their contribution to the peer review of this work. A peer review file is available.

Reprints and permissions information is available at <http://www.nature.com/reprints>

Publisher's note Springer Nature remains neutral with regard to jurisdictional claims in published maps and institutional affiliations.

Open Access This article is licensed under a Creative Commons Attribution-NonCommercial-NoDerivatives 4.0 International License, which permits any non-commercial use, sharing, distribution and reproduction in any medium or format, as long as you give appropriate credit to the original author(s) and the source, provide a link to the Creative Commons licence, and indicate if you modified the licensed material. You do not have permission under this licence to share adapted material derived from this article or parts of it. The images or other third party material in this article are included in the article's Creative Commons licence, unless indicated otherwise in a credit line to the material. If material is not included in the article's Creative Commons licence and your intended use is not permitted by statutory regulation or exceeds the permitted use, you will need to obtain permission directly from the copyright holder. To view a copy of this licence, visit <http://creativecommons.org/licenses/by-nc-nd/4.0/>.

© The Author(s) 2025